Peripheral sensory stimulation elicits global slow waves by recruiting somatosensory cortex bilaterally

Zachary P. Rosenthal[a,b,c,1], Ryan V. Raut[b,d], Ryan M. Bowen[c,e], Abraham Z. Snyder[c,d], Joseph P. Culver[d,e,f], Marcus E. Raichle[c,d,e], and Jin-Moo Lee[c,d,e,1]

[a]Medical Scientist Training Program, Washington University School of Medicine, St. Louis, MO 63110; [b]Graduate Program of Neuroscience, Washington University School of Medicine, St. Louis, MO 63110; [c]Department of Neurology, Washington University School of Medicine, St. Louis, MO 63110; [d]Department of Radiology, Washington University School of Medicine, St. Louis, MO 63110; [e]Department of Biomedical Engineering, Washington University School of Medicine, St. Louis, MO 63110; and [f]Department of Physics, Washington University School of Medicine, St. Louis, MO 63110

Edited by Peter L. Strick, University of Pittsburgh, Pittsburgh, PA, and approved January 19, 2021 (received for review October 11, 2020)

Slow waves (SWs) are globally propagating, low-frequency (0.5- to 4-Hz) oscillations that are prominent during sleep and anesthesia. SWs are essential to neural plasticity and memory. However, much remains unknown about the mechanisms coordinating SW propagation at the macroscale. To assess SWs in the context of macroscale networks, we recorded cortical activity in awake and ketamine/xylazine-anesthetized mice using widefield optical imaging with fluorescent calcium indicator GCaMP6f. We demonstrate that unilateral somatosensory stimulation evokes bilateral waves that travel across the cortex with state-dependent trajectories. Under anesthesia, we observe that rhythmic stimuli elicit globally resonant, front-to-back propagating SWs. Finally, photothrombotic lesions of S1 show that somatosensory-evoked global SWs depend on bilateral recruitment of homotopic primary somatosensory cortices. Specifically, unilateral lesions of S1 disrupt somatosensory-evoked global SW initiation from either hemisphere, while spontaneous SWs are largely unchanged. These results show that evoked SWs may be triggered by bilateral activation of specific, homotopically connected cortical networks.

slow wave | propagation | somatosensory cortex

Slow waves (SWs) are the predominant cortical rhythm during nonrapid eye movement sleep and anesthesia (1, 2). Since they were first characterized three decades ago, SWs have been linked to a variety of brain functions, including memory consolidation (3–6), homeostatic synaptic plasticity (7), and grouping of other oscillatory events (8–10). Macroscopic recordings (scalp electroencephalogram [EEG]) have revealed that spontaneous global SWs occur approximately once per second (~1 Hz) and propagate in a stereotypical front-to-back topography through the entire cortex (11). Local electrophysiology has demonstrated that virtually every cortical neuron participates in traveling SWs, exhibiting phase-locked alternation between depolarization (up-state) and hyperpolarization (down-state) (12, 13). During low arousal states, global SWs occur spontaneously but may also be evoked by peripheral sensory stimulation, as well as direct electromagnetic and optogenetic stimulation of the cortex (14–18). However, much remains unknown about the large-scale circuits supporting SW generation and propagation.

Here, we investigate the role of the primary somatosensory cortex and its interhemispheric connections in the initiation and propagation of somatosensory-evoked SWs. To this end, we performed widefield optical imaging of cortical dynamics in awake and anesthetized mice expressing fluorescent calcium indicator GCaMP6f in pyramidal neurons. High-resolution mesoscopic imaging across the whole dorsal neocortex allows for a more-precise characterization of globally coherent waves of neural activity than conventional approaches for recording SWs (EEG or local electrophysiology). We demonstrate that unilateral somatosensory stimulation elicits bilateral waves that propagate in opposite directions depending on state (awake versus ketamine/xylazine anesthesia). Further, we show that the imposed rhythm of stimulation induces resonant activity locally in sensorimotor areas that remains focal in awake animals. In contrast, in anesthetized animals, rhythmic stimulation subsequently elicits SWs that spread globally in a front-to-back trajectory across the cortex. Finally, we use a photothrombotic stroke model to show that somatosensory-evoked global SWs depend on engagement of both ipsilateral and contralateral somatosensory cortex (S1). Unilateral photothrombosis of S1 disrupts global SWs evoked by peripheral stimulation of either hemisphere but spares the global spatiotemporal structure of spontaneous SWs outside of the perilesional area. These findings suggest a key role for bilateral recruitment of homotopically connected somatosensory cortices in initiating somatosensory-evoked global SWs and suggest potential mechanisms by which focal cortical injuries may influence global brain dynamics.

Results

Peripheral Somatosensory Stimulation Elicits Traveling Waves with State-Dependent, Opposite Trajectories. Optical imaging was performed on $n = 10$ *Thy1-GCaMP6f* mice fitted with cranial windows, permitting observation of cortical calcium dynamics through the intact skull as previously described (19). Imaging data were collected during 5 min of right whisker stimulation (Fig. 1*A*) using computer-triggered air puffs in 10 s blocks (5 s of puffs at 2 Hz, followed by 5 s of rest). Mice were then

Significance

Slow waves are the predominant feature of brain activity during sleep and anesthesia. Slow waves are associated with plasticity, memory consolidation, and other brain functions. However, much remains unknown about the brain circuits that coordinate slow wave propagation. Here, we demonstrate that somatosensory stimulation evokes bilateral activation of primary somatosensory cortices (S1). Under anesthesia, S1 activation is followed by a global, front-to-back cortical slow wave. Using a focal lesion model, we show that evoked global slow waves depend on bilateral S1 activation, whereas spontaneous slow wave initiation does not depend on S1. These results demonstrate the existence of mechanisms by which focal injury may disrupt brain network dynamics.

Author contributions: Z.P.R., R.V.R., A.Z.S., J.P.C., M.E.R., and J.-M.L. designed research; Z.P.R. and R.M.B. performed research; Z.P.R., R.V.R., and R.M.B. analyzed data; and Z.P.R., R.V.R., A.Z.S., J.P.C., M.E.R., and J.-M.L. wrote the paper.

The authors declare no competing interest.

This article is a PNAS Direct Submission.

This open access article is distributed under Creative Commons Attribution-NonCommercial-NoDerivatives License 4.0 (CC BY-NC-ND).

[1]To whom correspondence may be addressed. Email: rosenthalz@wustl.edu or leejm@wustl.edu.

This article contains supporting information online at https://www.pnas.org/lookup/suppl/doi:10.1073/pnas.2021252118/-/DCSupplemental.

Published February 17, 2021.

Downloaded at Palestinian Territory, occupied on December 2, 2021

www.manaraa.com

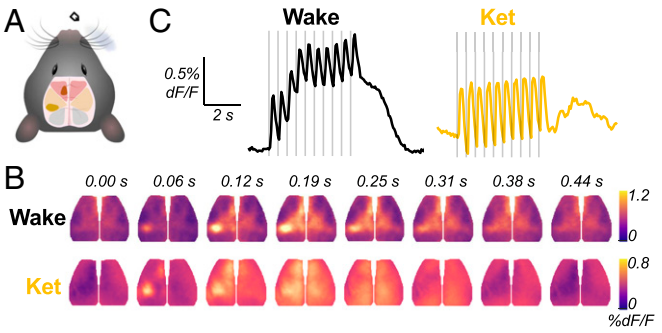

Fig. 1. Peripheral somatosensory stimulation elicits traveling waves with state-dependent, opposite trajectories. (*A*) A diagram of cortical field of view spanning frontal/motor (red), somatosensory (yellow), and visual (blue). Right whisker stimulation elicits activity in $S1_W$ (solid yellow) and $M1_W$ (solid red). (*B*) Still frames depicting group-averaged response to a single right whisker deflection during wake (n = 10 mice, 600 blocks) and ketamine/xylazine anesthesia (abbreviated "Ket," n = 9 mice, 540 blocks). The frames come from corresponding Movie S1. (*C*) A group-averaged time series of global GCaMP activity. The vertical lines indicate individual puff stimuli.

anesthetized with ketamine/xylazine, and the same stimulation protocol was repeated. Evoked responses were block averaged for awake (n = 10 mice, 600 blocks) and anesthetized (n = 9 mice, 540 blocks) conditions (Movie S1).

Fig. 1*B* shows the group-averaged response to a single puff in each condition. In awake animals, right whisker stimulation elicits activity focally in the left S1 whisker barrel cortex ($S1_W$) followed by a traveling wave spreading rostrally from $S1_W$ up to the whisker motor cortex, consistent with prior reports employing voltage-sensitive dye imaging in awake mice in a single hemisphere (17, 20). By expanding the field of view to include both hemispheres, we further demonstrate that this broad, rostrally propagating wave is mirrored in the contralateral sensorimotor cortex in awake animals (Fig. 1*B*). Under ketamine/xylazine anesthesia, whisker stimulation elicits a similar local response bilaterally in the sensorimotor cortex that is promptly subsumed by a global SW propagating caudally to the visual cortex. Block-averaged time series reveal that activity reverberates for several seconds after stimulation ceases in anesthetized but not awake animals (Fig. 1*C* and Movie S1). This suggests that spontaneous global SWs are briefly phase-reset by preceding stimulation, similar to prior reports (21, 22).

We characterized the spatiotemporal structure of cortical activity by examining dominant patterns of global coherence (*SI Appendix*, Fig. S1). We applied spatial singular value decomposition (SVD) to the frequency domain representation [i.e., space-frequency SVD (23)] of the group-averaged responses, yielding a set of orthogonal spatial modes containing global magnitude and phase information at each frequency (see *Materials and Methods*). Consistent with the patterns observed in Fig. 1*B*, opposing wave trajectories in wake (back-to-front) and anesthesia (front-to-back) are evident from the phase maps of the dominant spatial mode at 2 Hz in each condition (*SI Appendix*, Fig. S1*A*). Notably, the state-dependent changes in rostral/caudal directionality of stimulus-evoked waves mirrors previously reported findings in spontaneous activity during wake and anesthesia (24).

Rhythmic Stimulation Shifts the Dominant Frequency of SW Activity Globally Across the Dorsal Neocortex. The emergence of broadly propagating, stimulation-evoked SWs suggests that rhythmic somatosensory input may induce resonant activity globally across the cortex under anesthesia. To investigate this further, we asked whether stimulation shifts the dominant frequency of cortical activity and to what extent stimulation-evoked activity is globally coherent.

We first examined spectral power in whole runs of alternating 5-s blocks with stimulation ON or OFF to capture both spontaneous and evoked activity. As in local field potential recordings (25), spontaneous resting-state GCaMP dynamics exhibit a 1/f power spectrum. Under ketamine anesthesia, a prominent spectral peak emerges at 1- to 1.5-Hz that corresponds to spontaneous front-to-back SWs (19, 24). Here, we likewise observe that spontaneous 1- to 1.5-Hz SWs occur under anesthesia with front-to-back topography during interstimulus OFF periods (*SI Appendix*, Fig. S1*B*).

Importantly, by stimulating at a frequency faster than the endogenous SW frequency, we are able to dissociate unique properties of spontaneous SWs emanating from the frontal cortex (1 to 1.5 Hz, *SI Appendix*, Fig. S1*B*) from evoked SWs initiated in S1 (2 Hz, *SI Appendix*, Fig. S1*A*), which may be coordinated by distinct pathways. In order to determine whether the dominant frequency of global SW activity changes during ON periods of rhythmic stimulation, we computed the global average brain signal within each mouse and generated power spectrograms using a short-time Fourier transform (STFT). We observed that, under ketamine/xylazine anesthesia, global dynamics alternate between primarily 1- to 1.5-Hz oscillations during 5-s stim-OFF periods (corresponding to spontaneous SWs) and 2-Hz oscillations during 5-s stim-ON periods (corresponding to the imposed stimulation rhythm) (Fig. 2*A*). Averaging STFT spectra across ON and OFF blocks in anesthetized animals (Fig. 2*B*), we observed that OFF block power spectra look identical to those we have previously reported for spontaneous activity under anesthesia (24), while stimulation during ON blocks elicits a relative increase in global power at 2 Hz ($^{***}P$ = 0.0001) in tandem with a significant decrease in 1- to 1.5-Hz power ($^{****}P$ = 6.7e-5). Thus, during rhythmic stimulation under anesthesia, spontaneous SW power is suppressed while evoked power at the imposed stimulation frequency is enhanced. In contrast, in the awake state when SWs are absent, 2-Hz global power increases ($^{***}P$ = 0.0001), but 1- to 1.5-Hz power is not significantly changed (^{NS}P = 0.079).

Next, we examined whether stimulation-evoked resonance spreads more globally under anesthesia. First, we computed pixelwise power spectra over block-averaged time series and observed that, under anesthesia, evoked 2-Hz power is indeed globally distributed across the whole cortex. In contrast, in awake animals, 2-Hz power is largely restricted to the whisker barrel cortex and motor cortex (Fig. 2*C*). Similarly, the magnitude topography of the dominant spatial mode derived from space-frequency SVD shows more global effects under anesthesia (*SI Appendix*, Fig. S1*A*). To quantify this phenomenon further, we calculated global coherence of evoked (2-Hz) and spontaneous (1- to 1.5-Hz) SWs as the fractional power of the leading spatial mode obtained from space-frequency SVD [i.e., the proportion of global coherence explained by the first SVD component (23, 26)]. Indeed, global coherence of evoked 2-Hz waves is significantly greater under ketamine anesthesia than during wake ($^{**}P$ = 0.0028, Fig. 2*D*). As expected, with the emergence of spontaneous global SWs, the leading spatial mode of 1- to 1.5-Hz activity is more broadly distributed in magnitude maps (*SI Appendix*, Fig. S1*B*) and more globally coherent under ketamine anesthesia than in the awake state (Fig. 2*D*, $^{***}P$ = 0.0005).

Unilateral Ablation of S1 Reduces the Global Coherence of Somatosensory-Evoked SWs. The above-described results demonstrate that unilateral somatosensory stimulation under anesthesia elicits a focal response in S1 followed by a global,

Downloaded at Palestinian Territory, occupied on December 2, 2021

www.manaraa.com

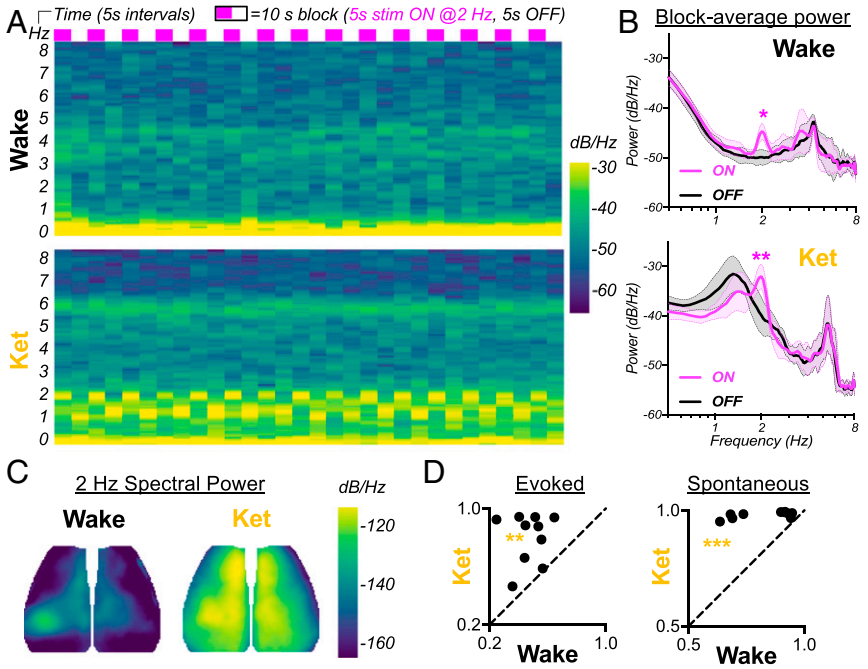

Fig. 2. Rhythmic stimulation shifts the dominant frequency of SW activity globally across the dorsal neocortex. (*A*) Group-averaged spectrograms of global GCaMP power (0 to 8 Hz, *y*-axis) over the course of consecutive 10-s blocks consisting of 5-s stim ON and 5-s stim OFF (time in 5-s bins, *x*-axis). (*B*) Average power spectra for all stim-ON (magenta) and stim-OFF (black) periods, computed by averaging across all ON or OFF windows from spectrograms in *A*. The differences are statistically tested by paired *t* test. Note, spectral peaks at ~4 Hz (wake) and ~5.5 Hz (ketamine) correspond to heartrate. The spectra are not variance normalized to permit comparison of changes in absolute power. The broad peak widths reflect biological variance, as well as the brief period for computing the Fourier transform. (*C*) Cortical maps depicting spatial distribution of 2-Hz power, computed from the group-averaged block. (*D*) The global coherence of evoked (2-Hz) and spontaneous (1- to 1.5-Hz) activity, comparing wake versus ketamine. The global coherence is calculated within individual mice as the fractional power of the leading spatial mode obtained from space-frequency SVD (23, 26). The statistical significance is determined by paired *t* test.

front-to-back SW. This sequence is consistent with several possibilities and does not necessarily indicate causality for S1 triggering the global SW (15, 27). If the global SW component is triggered in parallel with S1 activation via direct input from subcortical circuits onto frontal/prefrontal regions, one may expect the global SW component to be independent of S1 activation. Alternatively, the front-to-back SW may be initiated via direct or indirect connectivity between the frontal cortex and the S1 contralateral to stimulation. Lastly, given that unilateral stimulation elicits bilateral responses in S1 at baseline (albeit more weakly in ipsilateral S1), a third possibility is that paired activation of both somatosensory cortices—likely involving their recurrent interaction—is necessary for triggering global SWs.

To disambiguate these possibilities, we analyzed a previously collected dataset in which responses to 3-Hz forepaw stimulation under ketamine/xylazine anesthesia were examined before ("pre") and 1 wk following ("post") unilateral laser photothrombosis of forepaw sensory cortex ($S1_{FP}$) (28). These infarcts have well-circumscribed margins and are confined within the left hemisphere $S1_{FP}$ cortex (Fig. 3*A*) with an estimated volume of 1.94 ± 0.33 mm^3. Imaging was performed during 5 min of stimulation of the right or left forepaw, under anesthesia, using mild cutaneous electrical shock in 20-s blocks (5 s of shocks at 3 Hz, followed by 15 s of rest). Results represent an average of $n = 12$ mice, 180 blocks total per paw at each timepoint.

At baseline, 3-Hz electrical stimulation of the right or left forepaw elicits contralateral $S1_{FP}$ and motor responses followed by a global, front-to-back SW (Fig. 3*B* and Movies S2 and S3), similar to responses following whisker stimulation (Fig. 1). One week after left $S1_{FP}$ stroke, right forepaw stimulation on average evokes a weaker left $S1_{FP}$ response, as expected due to local tissue death (visible as a dark circular void in Fig. 3*B*). Furthermore, the subsequent global wave of activity evoked by right paw stimulations is also dramatically attenuated: secondary activation of the ipsilateral motor cortex and contralateral sensorimotor cortex are weaker, and the ensuing global front-to-back SW is reduced in amplitude.

Stimulating the left forepaw after left $S1_{FP}$ stroke still elicits a similar amplitude response in the right $S1_{FP}$ and motor cortex in the contralesional hemisphere on average; however, surprisingly, the subsequent global SW component is again weakened (Fig. 3*B*). While the dominant spatial modes exhibit similar propagation patterns pre- and poststroke (Fig. 3 *C* and *D*), global coherence of evoked SWs was significantly reduced after stroke for both contralesional (left paw $^*P = 0.02$, Fig. 3*E*) and ipsilesional (right paw $^*P = 0.03$, Fig. 3*F*) stimulation. Importantly, these changes are specific to somatosensory-evoked SWs. In contrast, global coherence of spontaneous SWs was strong and not significantly altered from prestroke baseline during OFF periods of left paw ($^{NS}P = 0.85$, Fig. 3*E*) and right paw ($^{NS}P = 0.15$, Fig. 3*F*) stimulation runs. Thus, unilateral ablation of S1 reduces global coherence of somatosensory-evoked SWs but not spontaneous SWs.

Unilateral Ablation of S1 Disrupts Globally Resonant Evoked SWs in Both Hemispheres. Next, we tested whether the spatial distribution of SW resonance is altered following unilateral stroke in $S1_{FP}$. As in Fig. 2*C*, we mapped group-averaged, 3-Hz evoked SW power during stimulation to the left (Fig. 4*A*) or right forepaw (Fig. 4*B*) pre- and poststroke. We then subtracted these maps to assess the relative change in 3-Hz evoked SW power and quantified total power change in the left (excluding the infarct) and right

Downloaded at Palestinian Territory, occupied on December 2, 2021
www.manaraa.com

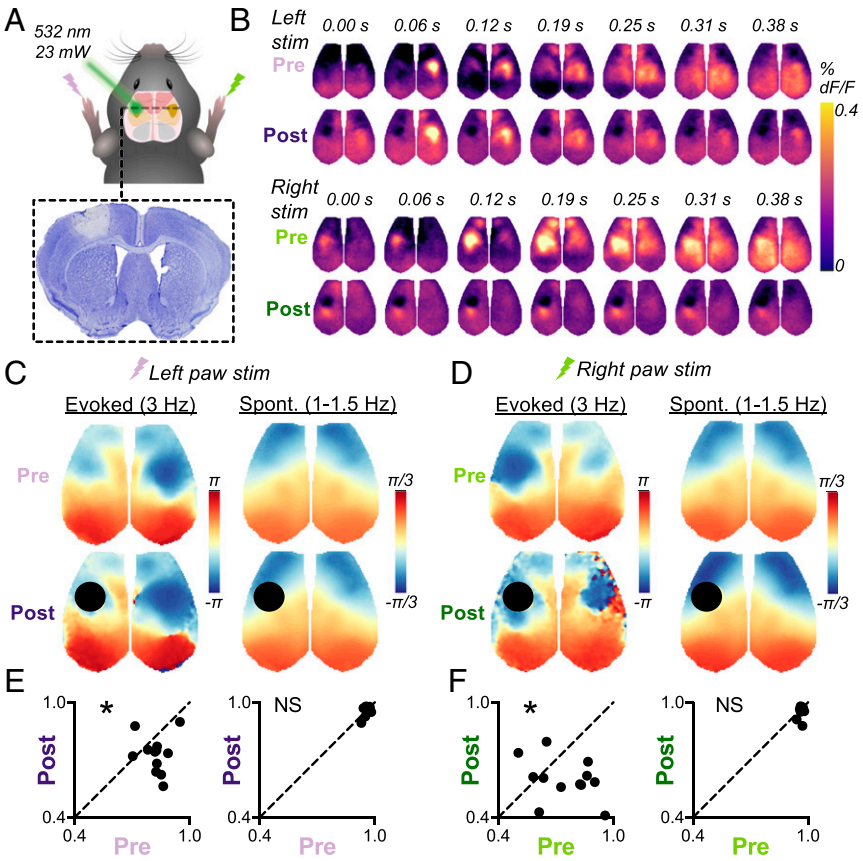

Fig. 3. Unilateral ablation of S1 reduces global coherence of 3-Hz somatosensory-evoked SWs but not 1- to 1.5-Hz spontaneous SWs. (*A*) A diagram depicting photothrombosis of the left forepaw somatosensory cortex ($S1_{FP}$, plotted bilaterally in solid yellow) along with a Nissl-stained cross-section through the middle of the infarct used to calculate infarct volume. Cell death is isolated within $S1_{FP}$ cortex. (*B*) The still frames depicting group-averaged response to right paw stimulation pre- (light green) and poststroke (dark green) as well as left paw stimulation pre- (pale purple) and poststroke (dark purple). The data represent an average of $n = 12$ mice, 180 blocks total per paw at each timepoint. The frames come from corresponding Movie S2 (right paw stimulation) and Movie S3 (left paw stimulation). (*C* and *D*) Dominant spatial mode phase maps of evoked (3-Hz) and spontaneous (1- to 1.5-Hz) SWs derived from space-frequency SVD of group-averaged blocks of left paw stimulation (*C*) and right paw stimulation (*D*). The early portions of global waves exhibit negative phase values and late portions exhibit positive values (units are in radians). (*E* and *F*) The global coherence of evoked and spontaneous SWs during runs of left (*E*) or right (*F*) paw stimulation, comparing pre- and poststroke within individual mice with a paired *t* test. The quantification of global coherence excluded the infarct (masked in black) to capture changes in surviving cortex.

hemispheres (Fig. 4 *C* and *D*). Compared to baseline, right paw stimulation after stroke resulted in a significantly weaker increase in power at the stimulation frequency (3 Hz) in both hemispheres (Fig. 4 *B* and *D*, $^{**}P = 0.0094$ in the left hemisphere, $^{**}P = 0.0075$ in the right). Left paw stimulation provided more informative responses: 3-Hz evoked SW power was significantly reduced across the left (ipsilesional) hemisphere (Fig. 4 *A* and *C* $^{**}P = 0.0091$). Notably, left paw stimulation generated 3-Hz evoked SW power within the right (contralesional) $S1_{FP}$ at similar levels to baseline, but global power in the rest of the right hemisphere was reduced. On average, right hemisphere power was unchanged (Fig. 4*D*, $^{NS}P = 0.16$).

In addition, we tested whether unilateral stroke in $S1_{FP}$ would disrupt SWs evoked via other somatosensory modalities (*SI Appendix*, Fig. S2). Using a new cohort of mice, we recorded evoked responses to 3-Hz whisker stimulation before and after photothrombosis of neighboring forepaw S1 ($n = 11$ mice, 165 blocks total per timepoint). We found that whisker-evoked SWs were spared by injury in $S1_{FP}$. While there were focal areas of reduced evoked 3-Hz power in the left motor cortex ($M1_W$), global 3-Hz whisker evoked SW power was unchanged in both hemispheres overall (*SI Appendix*, Fig. S2 *A* and *B*, $^{NS}P = 0.70$ in the left hemisphere, $^{NS}P = 0.16$ in the right). Consistent with this finding, the dominant spatial mode evoked by 3-Hz whisker stimulation exhibits similar spatial topography and global coherence before and after photothrombosis in $S1_{FP}$ (*SI Appendix*, Fig. S2 *C* and *D*, $^{NS}P = 0.34$).

Lastly, we examined spontaneous SW power (1 to 1.5 Hz) during stim-OFF epochs, extracted from whole runs without block averaging. We found that spontaneous SWs exhibit less power perilesionally (i.e., in the ring of surviving cortex immediately contiguous to the lesion) but not globally (*SI Appendix*, Fig. S3). During right paw stim-OFF epochs, left hemisphere spontaneous SW power was significantly decreased after stroke ($^{**}P = 0.0036$), primarily in the perilesional area, while right hemisphere SW power was unchanged overall ($^{NS}P = 0.20$). During left paw stim-OFF epochs, left hemisphere spontaneous SW power was significantly reduced ($^{**}P = 0.0044$), again observed primarily in the perilesional area, while right hemisphere SW power was unchanged overall ($^{NS}P = 0.45$). Thus, unilateral ablation of S1 reduces global resonance of somatosensory-evoked SWs initiated in S1 in either hemisphere but not that of spontaneous SWs.

Discussion

Over the last three decades, research on anatomic circuitry underlying SWs has largely focused on untangling the contributions

Downloaded at Palestinian Territory, occupied on December 2, 2021

www.manaraa.com

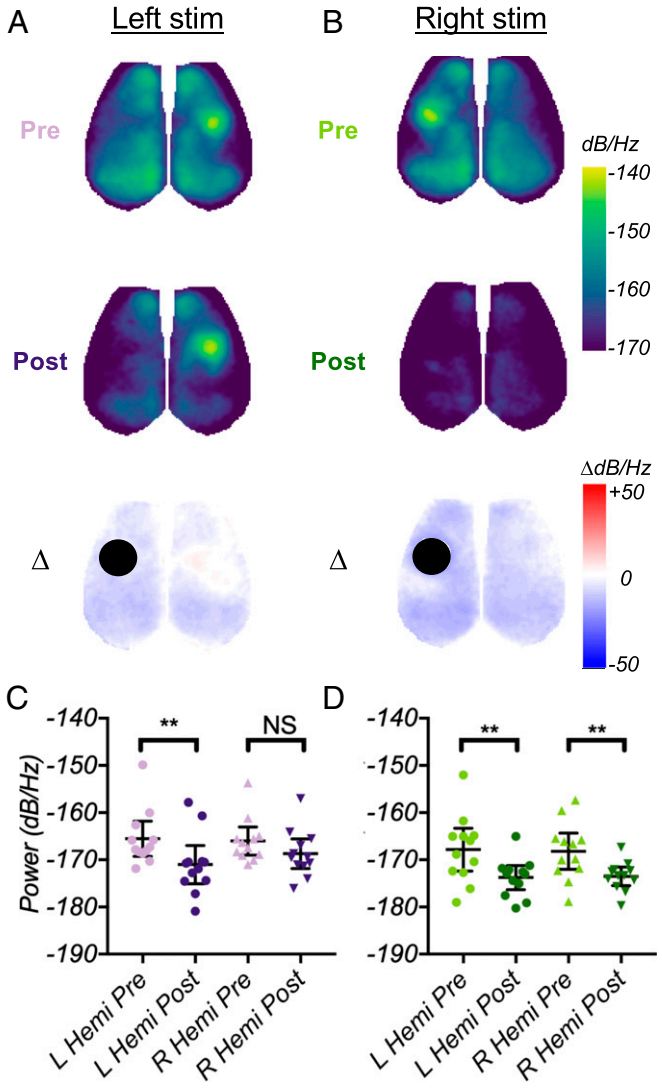

Fig. 4. Unilateral ablation of S1 disrupts global resonance of evoked 3-Hz SWs in both hemispheres. (*A* and *B*) Cortical maps of 3-Hz evoked SW power, computed from group-averaged blocks, pre- and poststroke (and Δ between them) for left (*A*) and right (*B*) paw stimulation. (*C* and *D*) The quantification of 3-Hz power change averaged within left and right hemispheres for left (*C*) and right (*D*) paw stimulation pre- versus poststroke. A two-way ANOVA with Sidak's multiple comparison test was used to confirm significant differences within individual mice. The quantification in *C* and *D* excludes the infarct to capture changes in surviving cortex.

of the cortex versus the thalamus (9). These investigations have primarily relied on local electrophysiological recordings. As a result, broader questions about how these circuits contribute to global propagation within large-scale cortical networks have received less attention. Here, we use widefield optical neuroimaging to investigate how specific cortical modules contribute to global propagation. In particular, we ask how does the primary somatosensory cortex contribute to somatosensory-evoked global SWs?

Our results suggest that global SWs in response to unilateral somatosensory stimulation require bilateral somatosensory cortices. Specifically, we observe the following: 1) somatosensory stimulation induces traveling waves emanating from bilateral S1 with state-dependent trajectories; 2) under anesthesia, rhythmic stimulation subsequently evokes resonant SWs front-to-back across the whole cortex at the imposed stimulation frequency; 3) unilateral lesioning of $S1_{FP}$ disrupts global SWs triggered by forepaw stimulation of either the ipsilesional or contralesional cortex; and 4) in contrast, ablation of $S1_{FP}$ spares spontaneous global SWs outside the perilesional area as well as SWs evoked by other somatosensory modalities. Taken together, these findings suggest that peripheral stimulation engages homotopically connected somatosensory cortices to initiate globally resonant SWs.

Our understanding of the circuitry supporting SWs is informed by the observation that SWs arise spontaneously but are also triggered by both peripheral and direct cortical stimulation. Spontaneous SWs have been shown to emanate primarily from prefrontal-orbitofrontal regions and propagate as front-to-back waves (11). However, spontaneous SWs also exhibit complex local trajectories in mice (29) and in humans (30, 31), which may vary during the process of falling asleep (32). Stimulation approaches have proven useful for dissecting the circuitry underlying observed patterns of cortical SWs. For example, transcranial magnetic stimulation during sleep induces SWs emanating from under the stimulating coil; this approach has revealed that sensorimotor regions elicit the most robust and reliable SWs (14). Indeed, S1 may be uniquely positioned to transmit local activity changes into global networks (33–35). Consistent with this finding, peripheral sensory stimulation in sleeping humans evokes activity with stereotypical topography: early responses in the sensory cortex specific to the stimulated modality, followed by a nonspecific, global, anterior-posterior K-complex SW (15). Intriguingly, evoked K complexes are coupled to wake-like increases in gamma power emerging from primary sensory areas which may serve as a potential driver of global SWs (36). However, whether activation of primary sensory areas is a necessary trigger for global SWs has remained an open question (15, 27). This dual response could be due to either parallel activation of specific (i.e., primary sensory) and nonspecific (i.e., frontal, prefrontal) pathways, or alternatively, initial activation of primary sensory areas propagating through cortico–cortical connections to trigger a global SW emanating from frontal regions. Disambiguating these possibilities is challenging with scalp EEG owing to limited spatial resolution and reliance on inverse source modeling (37).

Here, using a lesion model combined with widefield optical imaging of pyramidal calcium dynamics in mice, we provide evidence supporting a model in which front-to-back global SW coordination depends on initial local S1 responses. Specifically, we verify that whisker or forepaw stimulation elicits an early, local response in whisker or forepaw S1 which propagates toward the frontal cortex, followed by a front-to-back global SW (Figs. 1 and 3 and *SI Appendix*, Fig. S1). Lesioning S1 eliminates the local activation as well as the subsequent global slow SW (Fig. 4), indicating that primary sensory cortex activation is necessary to initiate sensory-evoked global waves. Future studies should investigate the role of direct and indirect connectivity between sensory and frontal cortices in triggering anterior-posterior waves, as well as determine the contributions of evoked SWs in maintaining vigilance versus sensory decoupling during sleep (38). In contrast to evoked SWs, we observe that spontaneous global SWs remain globally coherent (Fig. 3 *E* and *F*), and that their resonance remains intact outside of the perilesional area (*SI Appendix*, Fig. S3), indicating that spontaneous SWs are initiated by distinct circuits that do not require S1. Moreover, we observe that SWs evoked via a neighboring, intact somatosensory modality (whisker S1) exhibit no change in power or global coherence following the $S1_{FP}$ lesion (*SI Appendix*, Fig. S2), suggesting that SW initiation pathways are specific to a given modality or somatotopic region.

We further show that global SW initiation engages interhemispheric connectivity. Under ketamine/xylazine anesthesia,

Downloaded at Palestinian Territory, occupied on December 2, 2021

www.manaraa.com

somatosensory stimulation elicits SWs bilaterally in intact mice. In mice with unilateral S1 photothrombosis, global SW generation is disrupted following stimulation of either hemisphere (Figs. 3 and 4). This finding suggests that bilateral recruitment of and/or paired interaction between homotopic somatosensory cortices mediates global SW generation in response to stimulation, while a unilaterally intact S1 is insufficient to generate a global SW. Bilateral engagement may be mediated by direct callosal and/or indirect subcortical interhemispheric connections. A recent study in sleeping humans showed that severing the corpus callosum disrupts the interhemispheric spread of spontaneous SWs without changing the total amount of cortical SW activity (39). Thus, while callosal connectivity is necessary to synchronize activation of the two hemispheres, it does not appear to be necessary to trigger spontaneous SWs in either one separately. Likewise, SWs are bilaterally symmetric in wild-type mice but not in acallosal mice (29). In this context, our findings are consistent with a central role of interhemispheric connectivity in synchronizing SWs bilaterally, likely via the corpus callosum. Given that unilateral visual stimuli also elicit bilateral cortical activity (17), future studies may confirm that our findings generalize to SWs evoked by other sensory modalities.

We have previously shown that spontaneous global waves in the infraslow (<0.1 Hz) and delta (1- to 4-Hz) frequency bands exhibit stereotypical opposed trajectories that reverse direction between wake and anesthesia (24). Here, we extend those findings by showing that stimulation-evoked globally propagating delta band activity likewise exhibits predominantly posterior-to-anterior waves in awake animals but predominantly anterior-to-posterior SWs under anesthesia. Previous reports comparing evoked responses during wake and anesthesia have not addressed this phenomenon. One study reports no differences between stimulation-evoked wave patterns between wake and isoflurane-anesthetized states (17). The effects may be obscured by the use of isoflurane during craniotomy preps immediately prior to awake imaging as well as extraneous effects of isoflurane on abolishing normal connectivity patterns (40). Another voltage-sensitive dye study observed that whisker stimulation elicits spatially broad activations from S1 to M1 in both awake and urethane-anesthetized animals (20). Consistent with our findings, supplementary videos show that evoked global waves exhibit state-dependent changes in spatial trajectory (20). Future investigations may further our understanding of the state-dependence of sensory-evoked global waves in naturally sleeping animals, though it is practically challenging to evoke sensory stimulation while maintaining natural sleep. Though ketamine/xylazine anesthesia recapitulates many key features of natural sleep, anesthesia produces more homogenous, higher-amplitude SWs (41) and thus may represent a state in which SWs are enhanced beyond native physiology.

Our lesion experiment results imply a role for S1 and its intracortical connectivity in eliciting SWs. Alternatively, it is possible that the loss of global propagation is influenced by remote effects [e.g., secondary injury to corticothalamic connectivity (42)]. The role of the thalamus in cortical SWs has been historically controversial. Although the cortex is capable of intrinsically generating SWs without the thalamus (43–47), intact connectivity between the thalamus and cortex likely influences the expression of cortical SWs (48–51). Thus, the current consensus is that the cortex can intrinsically generate SW activity, but this activity is modulated by corticothalamic connectivity in vivo (9). In fact, several subcortical nuclei contribute to SWs in the intact brain, including the basal forebrain (52, 53), brainstem nuclei (9, 54, 55), and the claustrum (56). Further investigation will be required to determine whether focal cortical injury disrupts global SWs via loss of intracortical connectivity, subcortical connectivity, or both.

Another significant gap in our understanding of SWs lies in how they are disrupted by injuries such as stroke. Here, we observe that stroke in S1 does not just eliminate local activity but can also disrupt somatosensory-evoked global SWs. Photothrombosis produces highly focal, circumscribed lesions that provide insight into the effects of cortical death on SWs. However, this model does not recapitulate the graded ischemic injury observed in the penumbra of natural strokes. In the setting of a true ischemic penumbra, EEG studies in humans have demonstrated that SW sleep activity is increased around infarcts (57) in tandem with the emergence of pathological peri-infarct SWs during wakefulness (58). Thus, stroke may disrupt SWs by divergent mechanisms, both due to death of circuits generating SWs, as well as dysfunction in surviving neurons in the peri-infarct zone. These observations carry important implications for large-scale functional connectivity. Stroke has been shown to disrupt global functional connectivity (FC) in both humans (59–62) and rodents (63–65). Similar mechanisms may underlie SW dysfunction and large-scale FC changes (9, 66). Just as recovery of FC is predictive of stroke recovery, recovery of SW dynamics during rehabilitative therapy has likewise been shown to predict functional recovery (67). The present findings invite further investigation of the circuit mechanisms of SW physiology and dysfunction and suggest potential uses of SWs as a biomarker of brain network integrity.

Materials and Methods

Mouse Model. All procedures described below were approved by the Washington University Animal Studies Committee in compliance with the American Association for Accreditation of Laboratory Animal Care guidelines. Mice were raised in standard cages in a double-barrier mouse facility with a 12 h–12 h light/dark cycle and ad libitum access to food and water. All experiments used 10- to 12-wk-old males hemizygous for *Thy1-GCaMP6f* (JAX 024276) on a C57BL/6J background. Mice of this strain express GCaMP in pyramidal neurons, permitting widefield cortical imaging of excitatory calcium dynamics, which correlates well with multiunit activity (68–70). Pups were genotyped by PCR prior to experiments to confirm the presence of the *Thy1-GCaMP6f* transgene using the forward primer 5′-CATCAGTGCAGCAGAGCTTC-3′ and reverse primer 5′-CAGCGTATCCACATAGCGTA-3′.

Cranial Windowing. Mice received buprenorphine analgesia (0.03 mg/kg, subcutaneous) and were anesthetized with isoflurane (3% induction, 1.5% maintenance). Body temperature was maintained via a thermostatic heating pad. Mice were secured in a stereotactic frame. The scalp was shaved, sterilized with isopropyl alcohol and betadine scrub, locally washed with lidocaine, and then incised at midline and retracted. A custom Plexiglas window with pretapped screw holes for head fixation was attached to the skull using dental cement (C&B-Metabond, Parkell Inc.), completely containing the surgical opening.

Photothrombosis. Photothrombosis was performed as previously described (71). This protocol induces focal, well-circumscribed, and highly reproducible lesions (72). Briefly, mice ($n = 12$) were injected with Rose Bengal (6.7 mg/kg, intraperitoneal), and a green diode-pumped solid-state laser (532 nm, 23 mW) collimated to a 1-mm spot was stereotactically centered on the Paxinos coordinates of the forepaw sensory cortex (–2.2 mm in X, +0.05 mm in Y versus bregma) for 10 min (73). Cessation of blood flow was confirmed via laser Doppler.

Infarct Volume Histology. A separate cohort of three animals were killed 3 d after photothrombosis. Mice were deeply anesthetized with FatalPlus (Vortech Pharmaceuticals) and transcardially perfused with heparinized phosphate-buffered saline (PBS). The brains were removed and fixed in 4% paraformaldehyde for 24 h and transferred to 30% sucrose in PBS. After brains were saturated, they were snap frozen on dry ice and coronally sectioned (50 μm) on a sliding microtome. Sections were stored in 0.2 M PBS, 30% sucrose, and 30% ethylene glycol at –20 °C. For each brain, three sections (spaced 300 μm apart, spanning the infarct) were stained with cresyl violet. A blinded experimenter traced infarct margins in ImageJ to measure

Downloaded at Palestinian Territory, occupied on December 2, 2021
www.manaraa.com

infarct area. These measures were multiplied by distance between sections to estimate infarct volume.

Optical Imaging System. Widefield imaging of cortical calcium dynamics was performed as previously described (19). Briefly, sequential illumination was provided by four LEDs: the 454-nm (blue) LED was used for GCaMP excitation, while the 523-nm (green), 595-nm (yellow), and 640-nm (red) LEDs were used for hyperspectral oximetric imaging. The 523-nm LED was also used as an emission reference to remove hemoglobin confound in the fluorescence signal using a previously validated method (74). The acquisition framerate was set to 16 Hz per channel for whisker imaging studies and 16.81 Hz per channel for forepaw stroke experiments. For image acquisition, we used a cooled, frame-transfer Electron Multiplying Charge Coupled Device camera (iXon 897, Andor) with an 85-mm f/1.4 camera lens and 67-Hz framerate (Rokinon). The field of view was ~1 cm^2, covering most of the dorsal convexity of the cerebral cortex (78 μm × 78μm pixels).

Optical Imaging Recordings. Mice were acclimated to head fixation while secured in a comfortable black felt hammock until they resumed normal resting behavior (whisking, grooming, and relaxed posture). Mice were imaged while awake and/or while anesthetized via intraperitoneal injection with a mixture of ketamine (86.9 mg/kg) and xylazine (13.4 mg/kg). Animals were allowed 10 min for anesthetic induction with the plane of anesthesia measured by respiratory rate and loss of responsiveness to toe pinch. After induction, body temperature was maintained by a thermostatic heating pad with feedback via rectal probe (TCAT-2LV; HP-4M, Physitemp). Whisker stimulation in Figs. 1 and 2, S1 was performed in 10-min epochs using computer-controlled, 40-pounds-per-square-inch air puffs (Picospritzer, Parker Hannifin) in a block design (5 s of 2-Hz, 0.1-s puffs; 5 s rest; 60 blocks/10 min total per mouse, $n = 10$ mice for awake, $n = 9$ mice for anesthesia). Data from one ketamine whisker stimulation session was lost due to a file saving error. Stroke imaging sessions were conducted at baseline and 1 wk after photothrombosis in a separate set of experiments performed three years prior using 3-Hz stimulation. We note that evoked SW propagation speed and trajectory is similar regardless of the stimulation frequency or rhythmicity. At each imaging session, forepaw stimulation was delivered by transcutaneous electrical stimulation using microvascular clips (Roboz) in a block design (5 s rest; 5 s of 3-Hz, 1.0-mA, 0.3-ms electrical pulses; 10 s rest; 15 blocks/5 min per mouse × $n = 12$ mice). For *SI Appendix*, Fig. S2, whisker stimulation after forepaw stroke used the same block design as forepaw data in Figs. 3 and 4 (5 s rest; 5 s of 3-Hz, 0.1-s puffs; 10 s rest; 15 blocks/5 min per mouse × $n = 11$ mice).

Optical Imaging Signal Processing. A binary brain mask was manually drawn in MATLAB for each recording session in each mouse. All subsequent analyses were performed on pixels labeled as brain. Image sequences from each mouse (as well as the brain mask for each mouse) were affine transformed to Paxinos atlas space using the positions of bregma and lambda (73) and then spatially and temporally detrended as previously described (19). The GCaMP6 fluorescence signal (%dF/F) was corrected for varying concentrations of absorptive hemoglobin using 523-nm LED reflectance.

Optical Imaging ROIs. Regions of interest (ROIs) in the whisker barrel cortex ($S1_W$) and forepaw sensory cortex ($S1_{FP}$) were determined based on functional stimulus mapping from an independent cohort of 21 12-wk-old *Thy1-GCaMP6f* mice using the same stimulation paradigms as described above. Blocks were averaged within and between mice to generate an average peak response map. An evoked response ROI was defined by any pixels with amplitude >75% of the maximum pixel intensity of the peak response map. ROIs generated from this approach were used in subsequent analyses for averaging within functional territories. ROIs generated in this manner were affine registered to Paxinos atlas space and used to assess responses in subsequent analyses. Infarct ROIs were defined as pixels with >75% reduction of homotopic FC poststroke in awake resting-state data from the same animal. ROIs generated from this approach approximate post hoc measurements of infarct volume histology.

Space-Frequency SVD. Frequency-specific propagation structure and global coherence were characterized via SVD of optical imaging data in the frequency domain. Performing SVD on multitaper spectral estimates provides a computationally efficient strategy to spectrally smooth and decompose time series data (23, 26). Thus, K Slepian tapers of bandwidth W were applied to pixelwise Fourier transforms. The resulting space-frequency matrix was decomposed into K spatially orthogonal complex modes at each frequency f, each with coherence magnitude and phase information.

SVD was applied to full runs for spontaneous activity (time-bandwidth product $TW = 12$, $K = 22$ tapers; or block averages for evoked activity ($TW = 3$, $K = 5$)). Tapers results were robust to different parameter choices. Spontaneous and evoked were not directly compared. A single dominant spatial mode was observed in each condition; hence, analyses were restricted to the first SVD component. Note that complex singular vectors are unique up to a complex sign (i.e., a unit phase factor). Thus, dominant spatial modes were phase aligned by rotation in the complex plane according to a reference phase value (here, the global circular mean phase of the mode) prior to averaging across runs.

Following SVD, a measure of global coherence $C(f)$ is provided by the fractional power of (i.e., proportion of total variance in the coherence spectrum that is explained by) the first mode:

$$C(f) = \frac{\lambda_1^2(f)}{\sum_{k=1}^{K} \lambda_k^2(f)}. \quad [1]$$

Poststroke global coherence calculations excluded the infarct so as to capture changes in surviving cortex. Space-frequency SVD was implemented in MATLAB and incorporated software routines from the freely available Chronux package (75). Changes in global coherence between states were statistically tested within individual mice by paired two-tailed t test, with significance set at $P < \alpha = 0.05$.

Power Spectral Analysis. Global power spectrograms (Fig. 2*A*) were generated by computing the global average %dF/F signal across all brain pixels within each mouse/run, and then performing a STFT using a 5-s window with 0 overlap to capture the spectral signature of each individual 5-s ON or OFF period within each block. Spectrograms were computed within individual mice and then averaged across mice. Power spectra (Fig. 2*B*) were computed by averaging across all ON or OFF windows from spectrograms in Fig. 2*A*. Note, spectra were not variance normalized, allowing comparison of changes in absolute rather than relative band-limited power across conditions. Changes in power (at 2 Hz and summed between 1 to 1.5 Hz) between the ON and OFF spectra in Fig. 2*B* were analyzed by paired t test, with significance set at $P < \alpha = 0.05$. Block-averaged power maps (Figs. 2*C* and 4 *A* and *B* and *SI Appendix*, Fig. S2*A*) were generated by averaging the %dF/F signal across all blocks within each mouse/run and then computing power at each pixel using Welch's method. Power maps were averaged within each hemisphere for each mouse, and pre- versus poststroke changes were statistically tested by repeated measures one-way ANOVA with Sidak's multiple comparison test (comparing within individual mice across time points) with significance set at an adjusted $P < \alpha = 0.05$. Power was expressed in decibels/Hz using the following equation:

$$Power\left(\frac{dB}{Hz}\right) = 10\log_{10}(Power(a.u.)). \quad [2]$$

Experimental Design and Statistical Analysis. Histograms and spectra are plotted as group mean ± 95% CI error bars. Individual data points represent individual mice. Sample size and specific time points were selected on the basis of previous studies examining network connectivity changes in mice (34, 41, 71). Prism 8 software was used to perform statistical testing. Tests used for each analysis are underlined above. Data were verified to be normally distributed prior to statistical testing using the D'Agostino & Pearson normality test. Throughout, significance of P values is depicted as $^*P < 0.05$, $^{**}P < 0.01$, $^{***}P < 0.001$, and $^{****}P < 0.0001$.

Data Availability. Data for this paper are stored on our institutional storage cloud and will be freely available upon request, but due to institutional policy on cybersecurity, specific access links have to be generated upon request rather than persistent public links. The total data volume available is several terabytes in size.

ACKNOWLEDGMENTS. This work was supported by grants from the NIH (F31NS103275 to Z.P.R.; P30NS098577 and P01NS080675 to A.Z.S. and M.E.R.; R01NS099429 and R01NS090874 to J.P.C. and J.M.L.; and R37NS110699 to J.M.L.), American Heart Association (20PRE34990003 to Z.P.R.), and NSF (DGE-1745038 to R.V.R.).

Downloaded at Palestinian Territory, occupied on December 2, 2021

www.manaraa.com

1. M. Steriade, A. Nuñez, F. Amzica, A novel slow (< 1 Hz) oscillation of neocortical neurons in vivo: Depolarizing and hyperpolarizing components. *J. Neurosci.* **13**, 3252–3265 (1993).
2. A. Destexhe, D. Contreras, M. Steriade, Spatiotemporal analysis of local field potentials and unit discharges in cat cerebral cortex during natural wake and sleep states. *J. Neurosci.* **19**, 4595–4608 (1999).
3. L. Marshall, H. Helgadóttir, M. Mölle, J. Born, Boosting slow oscillations during sleep potentiates memory. *Nature* **444**, 610–613 (2006).
4. K. L. Hoffman *et al*., The upshot of up states in the neocortex: From slow oscillations to memory formation. *J. Neurosci.* **27**, 11838–11841 (2007).
5. H. V. Ngo, T. Martinetz, J. Born, M. Mölle, Auditory closed-loop stimulation of the sleep slow oscillation enhances memory. *Neuron* **78**, 545–553 (2013).
6. S. Binder *et al*., Transcranial slow oscillation stimulation during sleep enhances memory consolidation in rats. *Brain Stimul.* **7**, 508–515 (2014).
7. G. Tononi, C. Cirelli, Sleep and the price of plasticity: From synaptic and cellular homeostasis to memory consolidation and integration. *Neuron* **81**, 12–34 (2014).
8. B. P. Staresina *et al*., Hierarchical nesting of slow oscillations, spindles and ripples in the human hippocampus during sleep. *Nat. Neurosci.* **18**, 1679–1686 (2015).
9. G. T. Neske, The slow oscillation in cortical and thalamic networks: Mechanisms and functions. *Front. Neural Circuits* **9**, 88 (2016).
10. C. N. Oyanedel, E. Durán, N. Niethard, M. Inostroza, J. Born, Temporal associations between sleep slow oscillations, spindles and ripples. *Eur. J. Neurosci.*, 10.1111/ejn.14906 (2020).
11. M. Massimini, R. Huber, F. Ferrarelli, S. Hill, G. Tononi, The sleep slow oscillation as a traveling wave. *J. Neurosci.* **24**, 6862–6870 (2004).
12. M. Volgushev, S. Chauvette, M. Mukovski, I. Timofeev, Precise long-range synchronization of activity and silence in neocortical neurons during slow-wave oscillations [corrected]. *J. Neurosci.* **26**, 5665–5672 (2006).
13. A. Luczak, P. Barthó, S. L. Marguet, G. Buzsáki, K. D. Harris, Sequential structure of neocortical spontaneous activity in vivo. *Proc. Natl. Acad. Sci. U.S.A.* **104**, 347–352 (2007).
14. M. Massimini *et al*., Triggering sleep slow waves by transcranial magnetic stimulation. *Proc. Natl. Acad. Sci. U.S.A.* **104**, 8496–8501 (2007).
15. B. A. Riedner, B. K. Hulse, M. J. Murphy, F. Ferrarelli, G. Tononi, Temporal dynamics of cortical sources underlying spontaneous and peripherally evoked slow waves. *Prog. Brain Res.* **193**, 201–218 (2011).
16. A. Stroh *et al*., Making waves: Initiation and propagation of corticothalamic Ca2+ waves in vivo. *Neuron* **77**, 1136–1150 (2013).
17. M. H. Mohajerani *et al*., Spontaneous cortical activity alternates between motifs defined by regional axonal projections. *Nat. Neurosci.* **16**, 1426–1435 (2013).
18. A. Greenberg, J. K. Abadchi, C. T. Dickson, M. H. Mohajerani, New waves: Rhythmic electrical field stimulation systematically alters spontaneous slow dynamics across mouse neocortex. *Neuroimage* **174**, 328–339 (2018).
19. P. W. Wright *et al*., Functional connectivity structure of cortical calcium dynamics in anesthetized and awake mice. *PLoS One* **12**, e0185759 (2017).
20. I. Ferezou *et al*., Spatiotemporal dynamics of cortical sensorimotor integration in behaving mice. *Neuron* **56**, 907–923 (2007).
21. W. Chen, K. Park, Y. Pan, A. P. Koretsky, C. Du, Interactions between stimuli-evoked cortical activity and spontaneous low frequency oscillations measured with neuronal calcium. *Neuroimage* **210**, 116554 (2020).
22. A. Pigorini *et al*., Bistability breaks-off deterministic responses to intracortical stimulation during non-REM sleep. *Neuroimage* **112**, 105–113 (2015).
23. J. C. Prechtl, L. B. Cohen, B. Pesaran, P. P. Mitra, D. Kleinfeld, Visual stimuli induce waves of electrical activity in turtle cortex. *Proc. Natl. Acad. Sci. U.S.A.* **94**, 7621–7626 (1997).
24. A. Mitra *et al*., Spontaneous infra-slow brain activity has unique spatiotemporal dynamics and laminar structure. *Neuron* **98**, 297–305.e6 (2018).
25. B. Pesaran *et al*., Investigating large-scale brain dynamics using field potential recordings: Analysis and interpretation. *Nat. Neurosci.* **21**, 903–919 (2018).
26. P. P. Mitra, B. Pesaran, Analysis of dynamic brain imaging data. *Biophys. J.* **76**, 691–708 (1999).
27. M. Bellesi, B. A. Riedner, G. N. Garcia-Molina, C. Cirelli, G. Tononi, Enhancement of sleep slow waves: Underlying mechanisms and practical consequences. *Front. Syst. Neurosci.* **8**, 208 (2014).
28. Z. P. Rosenthal, "Recovery of cortical delta band functional connectivity after stroke" in *Society for Neuroscience Meeting* (Washington D.C, 2017).
29. M. H. Mohajerani, D. A. McVea, M. Fingas, T. H. Murphy, Mirrored bilateral slow-wave cortical activity within local circuits revealed by fast bihemispheric voltage-sensitive dye imaging in anesthetized and awake mice. *J. Neurosci.* **30**, 3745–3751 (2010).
30. M. Murphy *et al*., Source modeling sleep slow waves. *Proc. Natl. Acad. Sci. U.S.A.* **106**, 1608–1613 (2009).
31. Y. Nir *et al*., Regional slow waves and spindles in human sleep. *Neuron* **70**, 153–169 (2011).
32. F. Siclari *et al*., Two distinct synchronization processes in the transition to sleep: A high-density electroencephalographic study. *Sleep (Basel)* **37**, 1621–1637 (2014).
33. L. L. Gollo, J. A. Roberts, L. Cocchi, Mapping how local perturbations influence systems-level brain dynamics. *Neuroimage* **160**, 97–112 (2017).
34. Z. P. Rosenthal *et al*., Local perturbations of cortical excitability propagate differentially through large-scale functional networks. *Cereb. Cortex* **30**, 3352–3369 (2020).
35. K. C. R. Fox *et al*., Intrinsic network architecture predicts the effects elicited by intracranial electrical stimulation of the human brain. *Nat. Hum. Behav.* **4**, 1039–1052 (2020).
36. M. Laurino, A. Piarulli, D. Menicucci, A. Gemignani, Local gamma activity during non-REM sleep in the context of sensory evoked K-complexes. *Front. Neurosci.* **13**, 1094 (2019).
37. P. L. Nunez, R. Srinivasan, *Electric Fields of the Brain: The Neurophysics of EEG* (Oxford Univerity Press, Oxford, 2006).
38. T. Andrillon, S. Kouider, The vigilant sleeper: Neural mechanisms of sensory (de) coupling during sleep. *Curr. Opin. Physiol.* **15**, 47–59 (2020).
39. G. Avvenuti *et al*., Integrity of corpus callosum is essential for the cross-hemispheric propagation of sleep slow waves: A high-density EEG study in split-brain patients. *J. Neurosci.* **40**, 5589–5603 (2020).
40. Q. Bukhari, A. Schroeter, M. Rudin, Increasing isoflurane dose reduces homotopic correlation and functional segregation of brain networks in mice as revealed by resting-state fMRI. *Sci. Rep.* **8**, 10591 (2018).
41. L. M. Brier *et al*., Separability of calcium slow waves and functional connectivity during wake, sleep, and anesthesia. *Neurophotonics* **6**, 035002 (2019).
42. M. Aswendt *et al*., Lesion size- and location-dependent recruitment of contralesional thalamus and motor cortex facilitates recovery after stroke in mice. *Transl. Stroke Res.* **12**, 87–97 (2020).
43. M. V. Sanchez-Vives, D. A. McCormick, Cellular and network mechanisms of rhythmic recurrent activity in neocortex. *Nat. Neurosci.* **3**, 1027–1034 (2000).
44. I. Timofeev, F. Grenier, M. Bazhenov, T. J. Sejnowski, M. Steriade, Origin of slow cortical oscillations in deafferented cortical slabs. *Cereb. Cortex* **10**, 1185–1199 (2000).
45. F. Amzica, M. Steriade, Disconnection of intracortical synaptic linkages disrupts synchronization of a slow oscillation. *J. Neurosci.* **15**, 4658–4677 (1995).
46. M. Steriade, A. Nuñez, F. Amzica, Intracellular analysis of relations between the slow (< 1 Hz) neocortical oscillation and other sleep rhythms of the electroencephalogram. *J. Neurosci.* **13**, 3266–3283 (1993).
47. J. N. MacLean, B. O. Watson, G. B. Aaron, R. Yuste, Internal dynamics determine the cortical response to thalamic stimulation. *Neuron* **48**, 811–823 (2005).
48. A. Doi *et al*., Slow oscillation of membrane currents mediated by glutamatergic inputs of rat somatosensory cortical neurons: In vivo patch-clamp analysis. *Eur. J. Neurosci.* **26**, 2565–2575 (2007).
49. F. David *et al*., Essential thalamic contribution to slow waves of natural sleep. *J. Neurosci.* **33**, 19599–19610 (2013).
50. M. Sheroziya, I. Timofeev, Global intracellular slow-wave dynamics of the thalamocortical system. *J. Neurosci.* **34**, 8875–8893 (2014).
51. S. Zucca, V. Pasquale, P. Lagomarsino de Leon Roig, S. Panzeri, T. Fellin, Thalamic drive of cortical parvalbumin-positive interneurons during down states in anesthetized mice. *Curr. Biol.* **29**, 1481–1490.e6 (2019).
52. M. Xu *et al*., Basal forebrain circuit for sleep-wake control. *Nat. Neurosci.* **18**, 1641–1647 (2015).
53. Y. Oishi *et al*., Slow-wave sleep is controlled by a subset of nucleus accumbens core neurons in mice. *Nat. Commun.* **8**, 734 (2017).
54. C. Anaclet *et al*., The GABAergic parafacial zone is a medullary slow wave sleep-promoting center. *Nat. Neurosci.* **17**, 1217–1224 (2014).
55. Z. Zhang *et al*., An excitatory circuit in the perioculomotor midbrain for non-REM sleep control. *Cell* **177**, 1293–1307.e16 (2019).
56. K. Narikiyo *et al*., The claustrum coordinates cortical slow-wave activity. *Nat. Neurosci.* **23**, 741–753 (2020).
57. R. Poryazova *et al*., Topographic sleep EEG changes in the acute and chronic stage of hemispheric stroke. *J. Sleep Res.* **24**, 54–65 (2015).
58. S. Sarasso *et al*., Local sleep-like cortical reactivity in the awake brain after focal injury. *Brain* **143**, 3672–3684, 10.1093/brain/awaa338 (2020).
59. A. Baldassarre, L. E. Ramsey, J. S. Siegel, G. L. Shulman, M. Corbetta, Brain connectivity and neurological disorders after stroke. *Curr. Opin. Neurol.* **29**, 706–713 (2016).
60. A. R. Carter, G. L. Shulman, M. Corbetta, Why use a connectivity-based approach to study stroke and recovery of function? *Neuroimage* **62**, 2271–2280 (2012).
61. C. Grefkes, G. R. Fink, Reorganization of cerebral networks after stroke: New insights from neuroimaging with connectivity approaches. *Brain* **134**, 1264–1276 (2011).
62. R. M. Dijkhuizen, G. Zaharchuk, W. M. Otte, Assessment and modulation of resting-state neural networks after stroke. *Curr. Opin. Neurol.* **27**, 637–643 (2014).
63. M. P. van Meer *et al*., Recovery of sensorimotor function after experimental stroke correlates with restoration of resting-state interhemispheric functional connectivity. *J. Neurosci.* **30**, 3964–3972 (2010).
64. D. H. Lim, J. M. LeDue, M. H. Mohajerani, T. H. Murphy, Optogenetic mapping after stroke reveals network-wide scaling of functional connections and heterogeneous recovery of the peri-infarct. *J. Neurosci.* **34**, 16455–16466 (2014).
65. A. Q. Bauer *et al*., Optical imaging of disrupted functional connectivity following ischemic stroke in mice. *Neuroimage* **99**, 388–401 (2014).

Downloaded at Palestinian Territory, occupied on December 2, 2021

www.manaraa.com

66. G. Buzsáki, A. Draguhn, Neuronal oscillations in cortical networks. *Science* **304**, 1926–1929 (2004).
67. S. Sarasso *et al*., Plastic changes following imitation-based speech and language therapy for aphasia: A high-density sleep EEG study. *Neurorehabil. Neural Repair* **28**, 129–138 (2014).
68. H. Dana *et al*., Thy1-GCaMP6 transgenic mice for neuronal population imaging in vivo. *PLoS One* **9**, e108697 (2014).
69. M. C. Murphy, K. C. Chan, S. G. Kim, A. L. Vazquez, Macroscale variation in resting-state neuronal activity and connectivity assessed by simultaneous calcium imaging, hemodynamic imaging and electrophysiology. *Neuroimage* **169**, 352–362 (2018).
70. Y. Ma *et al*., Resting-state hemodynamics are spatiotemporally coupled to synchronized and symmetric neural activity in excitatory neurons. *Proc. Natl. Acad. Sci. U.S.A.* **113**, E8463–E8471 (2016).
71. A. W. Kraft, A. Q. Bauer, J. P. Culver, J. M. Lee, Sensory deprivation after focal ischemia in mice accelerates brain remapping and improves functional recovery through Arc-dependent synaptic plasticity. *Sci. Transl. Med.* **10**, eaag1328 (2018).
72. K. A. Maxwell, R. H. Dyck, Induction of reproducible focal ischemic lesions in neonatal mice by photothrombosis. *Dev. Neurosci.* **27**, 121–126 (2005).
73. K. B. J. Franklin, G. Paxinos, *The Mouse Brain in Stereotactic Coordinates* (Academic Press, New York, 2012).
74. Y. Ma *et al*., Wide-field optical mapping of neural activity and brain haemodynamics: Considerations and novel approaches. *Philos. Trans. R. Soc. Lond. B Biol. Sci.* **371**, 20150360 (2016).
75. H. Bokil, P. Andrews, J. E. Kulkarni, S. Mehta, P. P. Mitra, Chronux: A platform for analyzing neural signals. *J. Neurosci. Methods* **192**, 146–151 (2010).

Downloaded at Palestinian Territory, occupied on December 2, 2021

www.manaraa.com